

Slab morphology in the Cascadia fore arc and its relation to episodic tremor and slip

Pascal Audet,^{1,2} Michael G. Bostock,¹ Devin C. Boyarko,³ Michael R. Brudzinski,³ and Richard M. Allen⁴

Received 31 August 2008; revised 26 August 2009; accepted 16 November 2009; published 2 April 2010.

[1] Episodic tremor and slip (ETS) events in subduction zones occur in the general vicinity of the plate boundary, downdip of the locked zone. In developing an understanding of the ETS phenomenon it is important to relate the spatial occurrence of nonvolcanic tremor to the principal structural elements within the subduction complex. In Cascadia, active and passive source seismic data image a highly reflective, dipping, low-velocity zone (LVZ) beneath the fore-arc crust; however, its continuity along the margin is not established with certainty, and its interpretation is debated. In this work we have assembled a large teleseismic body wave data set comprising stations from northern California to northern Vancouver Island. Using stacked receiver functions we demonstrate that the LVZ is well developed along the entire margin from the coast eastward to the fore-arc basins (Georgia Strait, Puget Sound, and Willamette Valley). Combined with observations and predictions of intraslab seismicity, seismic velocity structure, and tremor hypocenters, our results support the thesis that the LVZ represents the signature of subducted oceanic crust, consistent with thermal-petrological modeling of subduction zone metamorphism. The location of tremor epicenters along the revised slab contours indicates their occurrence close to but seaward of the wedge corner. Based on evidence for high pore fluid pressure within the oceanic crust and a downdip transition in permeability of the plate interface, we propose a conceptual model for the generation of ETS where the occurrence and recurrence of propagating slow slip and low-frequency tremor are explained by episodic pore fluid pressure buildup and fluid release into or across the plate boundary.

Citation: Audet, P., M. G. Bostock, D. C. Boyarko, M. R. Brudzinski, and R. M. Allen (2010), Slab morphology in the Cascadia fore arc and its relation to episodic tremor and slip, *J. Geophys. Res.*, 115, B00A16, doi:10.1029/2008JB006053.

1. Introduction

[2] Episodic tremor and slip (ETS) events are transient deformation phenomena characterized by the synchronous occurrence of slow slip events and nonvolcanic tremor with regular recurrence intervals along plate boundary faults at lower crustal depths [Schwartz and Rokosky, 2007]. They were first identified in Cascadia [Dragert *et al.*, 2001; Rogers and Dragert, 2003] and Japan [Obara, 2002; Obara *et al.*, 2004], however, recent evidence suggests they occur in at least several other subduction zones worldwide. They appear to be the expression of propagating slow slip along the plate interface downdip of the locked zone, although

their triggering mechanism is not well understood [Schwartz and Rokosky, 2007]. Their association with fluid motion in the vicinity, but updip, of the wedge corner is suggested based on seismic evidence for elevated pore fluid pressure within the subducted oceanic crust [Kodaira *et al.*, 2004; Shelly *et al.*, 2006; Audet *et al.*, 2009]. Downdip of the wedge corner, a significant amount of water is transferred upward from the slab to the overlying lithosphere through oceanic crustal eclogitization and serpentinization of the mantle wedge [Bostock *et al.*, 2002; Kawakatsu and Watada, 2007]. This apparent transition in permeability of the plate boundary also coincides with the frictional stability transition zone from brittle (seismic) deformation to ductile (aseismic) creep. Recurrence intervals of ETS events are documented to fluctuate along the margin, and correlate with age and composition of overriding lithosphere [Brudzinski and Allen, 2007]. The proximity of ETS events with the assumed downdip limit of megathrust rupture and the potential influence of the upper plate on recurrence intervals render structural knowledge of the subduction zone complex a primary issue in earthquake and slip modeling [e.g., Dragert *et al.*, 2001; Szeliga *et al.*, 2008].

¹Department of Earth and Ocean Sciences, University of British Columbia, Vancouver, British Columbia, Canada.

²Now at Seismological Laboratory, Department of Earth and Planetary Science, University of California, Berkeley, California, USA.

³Department of Geology, Miami University, Oxford, Ohio, USA.

⁴Seismological Laboratory, Department of Earth and Planetary Science, University of California, Berkeley, California, USA.

[3] In Japan, the dense distribution of borehole seismometers has allowed accurate determination of tremor hypocenters on the plate interface near the wedge corner [Shelly *et al.*, 2006]. Shelly *et al.* [2007a] further showed that tremors can be explained as a swarm of small, low-frequency earthquakes occurring as shear faulting on the plate interface, a suggestion confirmed by moment tensor solutions [Ide *et al.*, 2007b]. In Cascadia, however, very few low-frequency earthquakes accompanying tremors have been reported, hampering the accurate determination of tremor hypocenters. In northern Cascadia, hypocenters calculated using the source-scanning algorithm [Kao and Shan, 2004; Kao *et al.*, 2005] and envelope cross correlations [McCausland *et al.*, 2005] have a wide depth range and do not focus on the inferred plate interface. Low-frequency earthquakes documented below southern Vancouver Island occur ~10 km shallower than the inferred top of the slab, within the so-called E layer [Kao *et al.*, 2009]. In contrast, polarizations of tremor-generated *S* waves and surface movement from GPS observations of slow slip events imply that ETS events are the manifestation of slow, shear slip on the plate interface [Dragert *et al.*, 2001; Wech and Creager, 2007; Szeliga *et al.*, 2008]. The amount of slip, and hence equivalent magnitude of a slow slip event as determined from GPS data, is dependent on the assumed location of the plate interface. In northern Cascadia, the precise location of the slab is a matter of much debate due to conflicting interpretations of different data sets.

[4] The most recent compilation of depth to the plate interface [McCrorry *et al.*, 2006] presents a steeply dipping, N-S striking subducting Juan de Fuca plate in southern and central Cascadia, that transitions into a shallower dip and NW-SE strike direction north of ~49°N. This compilation is based on numerous independent characterizations of slab structure, obtained mostly from active source seismic profiling (e.g., refraction, wide-angle reflection), and regional earthquake tomography [McCrorry *et al.*, 2006, and references therein]. The slab model is drawn as a smooth surface with constant dip between adjacent transects and profiles. In areas where overlapping data sets yield conflicting depth estimates, the data set that provides the smoothest contour is retained.

[5] A growing number of receiver function studies of subduction zones delivers additional important controls on structure. These studies document the presence of a dipping, low-velocity zone (LVZ) generally interpreted to be subducted oceanic crust. Examples include southern and northern Cascadia [Nabelek *et al.*, 1993; Rondenay *et al.*, 2001; Nicholson *et al.*, 2005; Audet *et al.*, 2008, 2009; Abers *et al.*, 2009], NE Japan [Kawakatsu and Watada, 2007], SW Japan [Yamauchi *et al.*, 2003; Shiomi *et al.*, 2004], Alaska [Ferris *et al.*, 2003; Rondenay *et al.*, 2008], Chile [Yuan *et al.*, 2000], Hellenic [Li *et al.*, 2003; Endrum *et al.*, 2004], and Mariana [Tibi *et al.*, 2008] subduction zones. In southern Cascadia, the top of the LVZ has been associated with the plate interface. In northern Cascadia, this feature coincides with the E layer, a highly reflective and conductive zone imaged with active source reflection and magnetotelluric data. The latter feature was first identified as the subducting oceanic crust [Clowes *et al.*, 1983; Kurtz *et al.*, 1986; Cassidy and Ellis, 1993], but was later interpreted to rep-

resent trapped fluids in the overriding continental crust [Green *et al.*, 1986; Hyndman, 1988], 5–10 km shallower than the depth to the top of oceanic crust, defined by McCrorry *et al.* [2006]. As Nicholson *et al.* [2005] argue, the similarity of receiver function signature in southern and northern Cascadia implies either that the LVZ is not subducted oceanic crust and the depth to the plate interface in southern Cascadia is significantly deeper than previously thought, or the LVZ is oceanic crust and its depth in northern Cascadia is significantly shallower than previously thought. Moreover, the lateral extent and variability of this feature along Cascadia has yet to be properly characterized.

[6] In this paper we have assembled a large and diverse broadband seismic data set comprising stations along the entire fore-arc margin, from northern California to northern Vancouver Island. We demonstrate that the LVZ is well developed along the margin from the coast eastward to the fore-arc basins (Georgia Strait, Puget Sound, Willamette Valley). Based on thermal and petrological arguments and previous results, we associate the LVZ with subducted oceanic crust and discuss the relations between slab morphology and the occurrence of ETS.

2. Data

2.1. Station Distribution

[7] Data for this study were obtained from multiple temporary and permanent networks of broadband seismic stations maintained by the Canadian National Seismological Network (CNSN), the POLARIS consortium, the Geological Survey of Canada, the Pacific Northwest Seismic Network (PNSN), the Northern California Seismic Network (NCSN), and the Transportable and Flexible Arrays of USArray (TA, FACES). We used data from a total of 106 broadband stations spanning the entire Cascadia fore-arc margin from northern California to northern Vancouver Island (Figure 1). Coverage is dense along four lines with station spacing of ≤20 km on average, and relatively sparse elsewhere (Figure 1). Line 1 and line 2 consist of a cross-shaped array of POLARIS broadband instruments deployed in two approximately perpendicular arms on northern Vancouver Island. One arm of the array (line 1) trends NW-SE (136° azimuth) in the direction parallel to strike and straddles the northern terminus of the subduction zone. The second arm (line 2) trends WSW-ENE (70° azimuth) perpendicular to strike, just north of the extension of the Nootka fault beneath Vancouver Island. Line 1 and line 2 are complemented by 5 stations from a previous deployment [Cassidy *et al.*, 1998], and 2 stations from the CNSN. Line 3 is composed of 12 POLARIS broadband stations complemented by 4 CNSN stations, and trends SW-NE (80° azimuth) across southern Vancouver Island and the Strait of Georgia [Nicholson *et al.*, 2005]. Line 4 is composed entirely of stations deployed in 1993–1994 as part of an IRIS-PASSCAL experiment by researchers at the Oregon State University, and consists of 25 seismometers distributed across central Oregon along a W-E trend (90° azimuth) [Nabelek *et al.*, 1993; Rondenay *et al.*, 2001]. Station spacing is approximately 5 km along line 4.

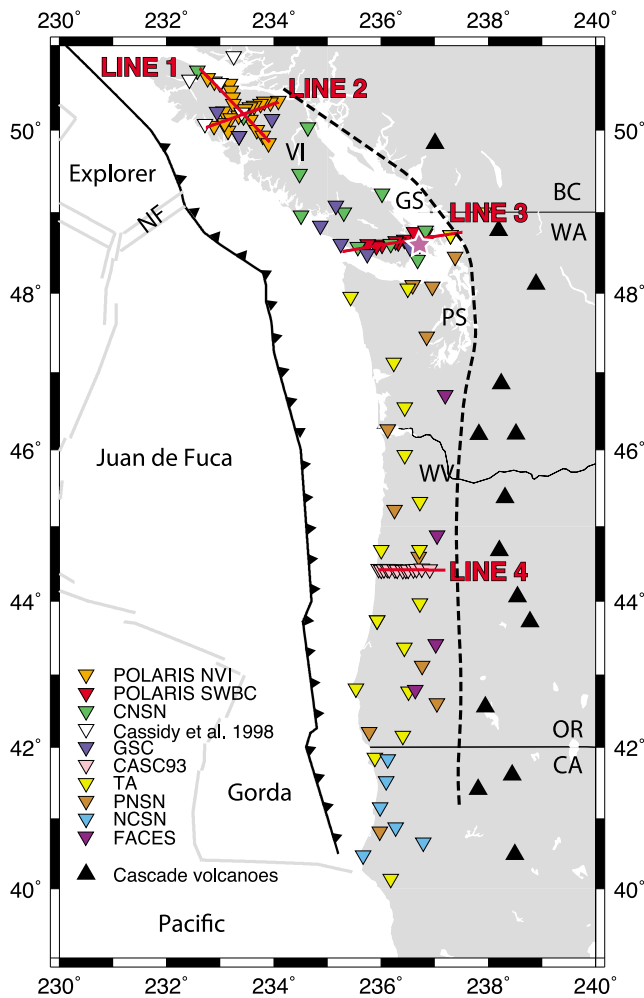


Figure 1. Map of the Cascadia subduction zone with broadband seismic stations located within the fore arc that were used in this study. The dashed line delineates the eastern limit of fore-arc lowlands (GS, Georgia Strait; PS, Puget Sound; WV, Willamette Valley). Black triangles indicate the location of active Cascade volcanoes. Solid black line with arrowheads represents the trench offshore, and grey lines are plate boundaries. The four lines discussed in section 4 are labeled in red. The purple star indicates the location of station PGC. NF, Nootka fault; VI, Vancouver Island; BC, British Columbia; WA, Washington; OR, Oregon; CA, California.

2.2. Preprocessing

[8] Three-component seismograms were collected for all events $M > 5.5$ in the epicentral distance range 30° – 100° . The vertical and horizontal (radial and transverse) components of motion are decomposed into upgoing P , S_V (radial), and S_H (transverse) wave components to partially remove the effect of the free surface [Bostock, 1998]. We retain seismograms with P component signal-to-noise ratios >10 dB over the first 10 s in the 0–2 Hz frequency band. Event coverage is dominated by the Western Pacific, Fiji-Tonga, and Central and South American corridors, with good back azimuthal coverage from 125° to 175° and from 225° to 40° , and less regularly sampled otherwise. Slab structure is

sampled mostly from the updip and strike parallel directions due to the dominantly N-S to NW-SE strike direction.

3. Methods

3.1. Receiver Functions

[9] Individual single-event seismograms are processed using the receiver function method, which employs the P component as an estimate of the source to deconvolve the S_V and S_H components and recover receiver-side S velocity structure. This procedure is performed using a Wiener spectral deconvolution [Bostock, 1998] with a regularization parameter calculated from the preevent noise spectrum. Receiver functions are subsequently filtered using a second-order Butterworth filter with corner frequencies defined below. The resulting S_V and S_H receiver function time series represent forward (P_{xS}) and back-scattered (P_{PxS} , P_{SxS}) waves from planar discontinuities in physical properties, identified by x (Figure 2). The timing and amplitude of each converted phase constrain overlying velocity structure (depth and V_P/V_S of the overlying column) and velocity contrasts at discontinuities, respectively.

[10] For isotropic, horizontal layering no energy is converted on the S_H component; energy on the S_H component must therefore represent either structural heterogeneity (e.g., dipping interface), anisotropy, or both [Frederiksen and Bostock, 2000]. In either case periodic polarity reversals of converted S_H phase amplitude with back azimuth are expected; for example, a plane dipping layer will produce a $1-\theta$ (360°) periodicity. In the case of anisotropy the patterns are more complicated due to the various degrees of symmetry of the elastic tensor and its orientation in space [Frederiksen and Bostock, 2000].

[11] To visualize coherent structural signals beneath individual stations we filter receiver functions between 0.1 and 0.35 Hz, sort by back azimuth of incoming wavefield, and display as blue-red color-coded traces (Figure 3). These data are sensitive to structures with scale lengths of 1–10 km and are dominated by the signature of an eastward dipping low-velocity zone. This signature includes 3 sets of oppositely polarized pulses comprising forward scattered P_{xS} conversions, and back-scattered P_{PxS} and P_{SxS} conversions from the top ($x = t$) and bottom ($x = b$) of the LVZ (Figure 2).

3.2. Phase Stacking

[12] To obtain precise point measurements of subsurface structure (depth of discontinuities and V_P/V_S of overlying structure) beneath each station, we adopt the stacking technique of Zhu and Kanamori [2000] for horizontal layering, and adapted by Rossi et al. [2006] to planar dipping layers. The procedure is based on stacking moveout-corrected traces for each weighted S_V and S_H converted phase (P_{xS} , P_{PxS} , P_{SxS}) in the receiver functions for a given model, and searching through a range of parameters for the model that maximizes the stacks. Strike direction along the margin can be constrained by polarity reversals on transverse component receiver functions in the absence of anisotropy. Alternatively, it can be directly estimated by calculating the normal of the plane tangent to the plate interface, based on the slab contours [McCroory et al., 2006]. Because most stations are too poorly sampled in back azimuth (Figures 3c and 3d) to constrain the $1-\theta$ periodicity, we chose the latter

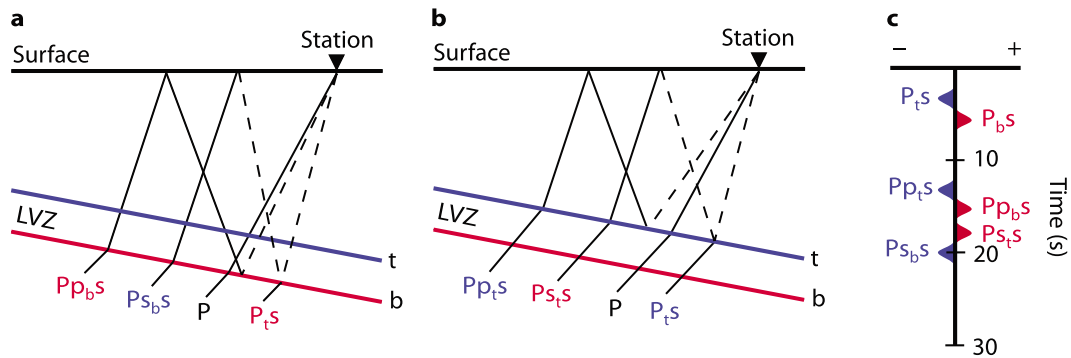


Figure 2. (a and b) Ray diagrams showing P to S converted phases and free surface multiples from an incident P wave interacting with a dipping low-velocity zone (LVZ) defined by top (t) and bottom (b) interfaces. Solid lines are rays traveling as P waves, and dashed lines are rays traveling as S waves. Red and blue fonts indicate positive and negative phase polarities, respectively. (c) Approximate radial receiver function corresponding to phases identified in Figures 2a and 2b. Each set of P to S conversions is generated twice from interactions at the top and bottom discontinuities, with opposite polarities.

method and corrected S_H polarities using predictions from the strike and dip of the subducted slab. Results are insensitive to inaccuracies in strike directions for shallow dips ($<20^\circ$).

[13] We use the phase-weighted stacking technique of Schimmel and Paulssen [1997] for stacking individual phase but employ the median instead of the mean to improve stack coherency. Our first target is the positive velocity contrast representing the Moho of the subducted oceanic plate

[Abers, 2005] because it is expected to represent the largest velocity contrast and thus produce the maximum amplitude in the stacks. We use a dipping, single-layer model with mantle and crustal P velocities of 7.8 and 6.5 km/s [Ramachandran et al., 2006] to compute traveltimes, although the results are only weakly dependent on this assumption [Zandt and Ammon, 1995]. Traveltimes are calculated from analytical solutions for a dipping interface [Audet et al., 2009].

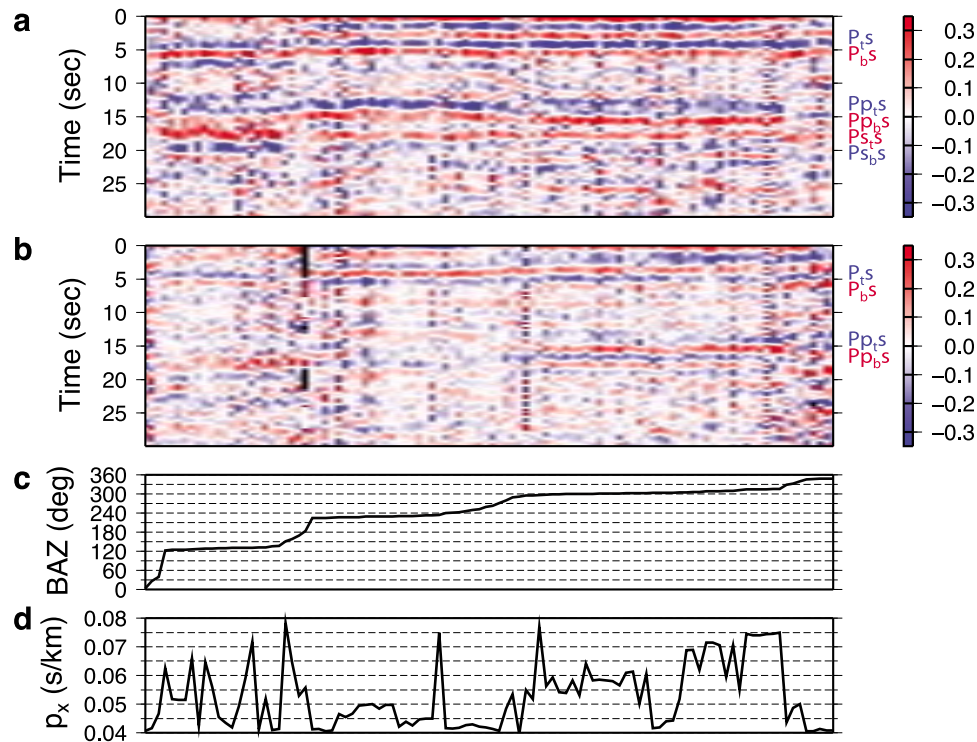


Figure 3. (a) Radial and (b) transverse component receiver functions at station PGC sorted by (c) back azimuth of incident wavefield. Amplitudes are relative to P component. Labels correspond to identified phases in Figure 2c. Transverse component phase arrivals in Figure 3b show polarity reversals and are more difficult to identify than their radial component counterparts in Figure 3a. (d) The distribution in horizontal slowness.

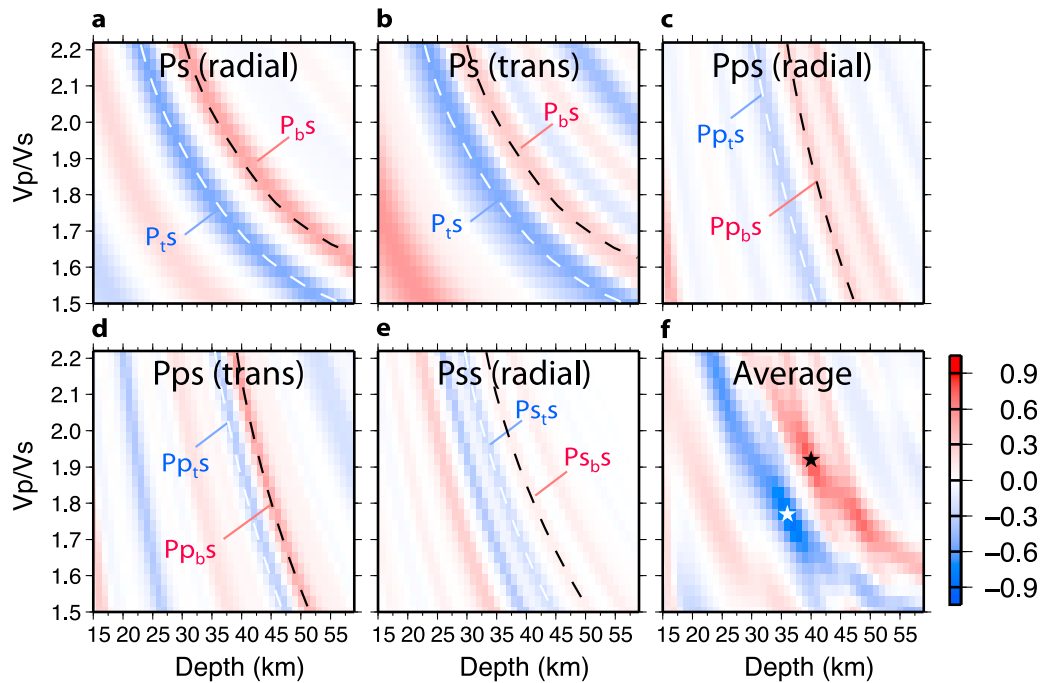


Figure 4. Example of phase stacking results for station PGC (Figure 3). (a–e) Stack plots for each scattered phase. Dashed lines indicate the maximum amplitude (or corresponding moveout curve) for the phase identified by labels. (f) Weighted average using a combination of phases in Figures 4a–4e as discussed in section 3.2. Note that polarities in Figure 4e have been reversed to produce constructive interference in Figure 4f. Amplitudes are relative to maximum in Figure 4f. In this realization the dip that produces optimal results is 14° . The minimum (white star) and maximum (black star) of the weighted average of each individual phase determines the depth to the top and bottom of the LVZ and representative V_p/V_s of overlying structure.

[14] Prior to stacking, we filter direct conversions at higher frequencies (0.1–1 Hz) than reverberations (0.1–0.5 Hz). We have found that such mixed frequency stacks produce more stable results than otherwise. Figure 4 shows the stacks for the individual scattered phases at station PGC. Visual inspection of these plots suggests that additional effects can bias the recovery of velocity structure. For example, the close proximity between the first (P_{PS}) and second (P_{SS}) reverberations implies that energy from both phases are not fully canceled by moveout corrections. The dual-polarity nature of the LVZ signals produces a second complication. It can be difficult to distinguish phases arising from top and bottom of the LVZ in individual stacks from those due to different scattering modes (Figures 4c–4e). In addition, transverse component stacks are generally less coherent than the corresponding radial component stacks, as they are more affected by anisotropy. For these reasons, the blind application of weighted averaging may produce erroneous results. Therefore, we generally use a combination of 2 to 3 phases (one forward scattered phase, and one or two reverberated phases) with equal weights, depending on the quality of the stacks and our ability to identify each scattered phase.

[15] The final stack at station PGC illustrates that in addition to recovery of depth and V_p/V_s from the strong positive maximum (bottom of the LVZ), we also retrieve the secondary, shallower and lower V_p/V_s , negative extremum from a negative velocity contrast at the top of the LVZ

(Figure 4f). This is true for most stations, and, in light of the analysis by Audet *et al.* [2009], suggests that the LVZ is generally characterized by much higher V_p/V_s than overlying material. Measurement of V_p/V_s within the LVZ, although possible for some stations, is difficult, and requires clear signals arising from sharp planar boundaries that can be extracted and analyzed at high frequencies (~ 2 Hz) [Audet *et al.*, 2009]. Most stations do not record sufficient data nor possess the requisite signal-to-noise ratio for this type of analysis. We will thus focus on the general observations of depth and V_p/V_s of the overlying crustal structure. Uncertainties (± 3 km) in depth to top and bottom of LVZ are estimated from the flatness of the stack around the solution [Zhu and Kanamori, 2000]. Analysis of formal errors based on the bootstrap method gives similar estimates [Audet *et al.*, 2009].

4. Results

4.1. Receiver Functions Along Dense Linear Arrays

[16] The dense station coverage along the four lines allows us to display receiver functions from adjacent stations as an image [e.g., Nicholson *et al.*, 2005; Mercier *et al.*, 2008] (Figure 5). Note that relative distances between stations are not preserved, however these plots are helpful in allowing unambiguous identification of laterally coherent signals associated with the slab.

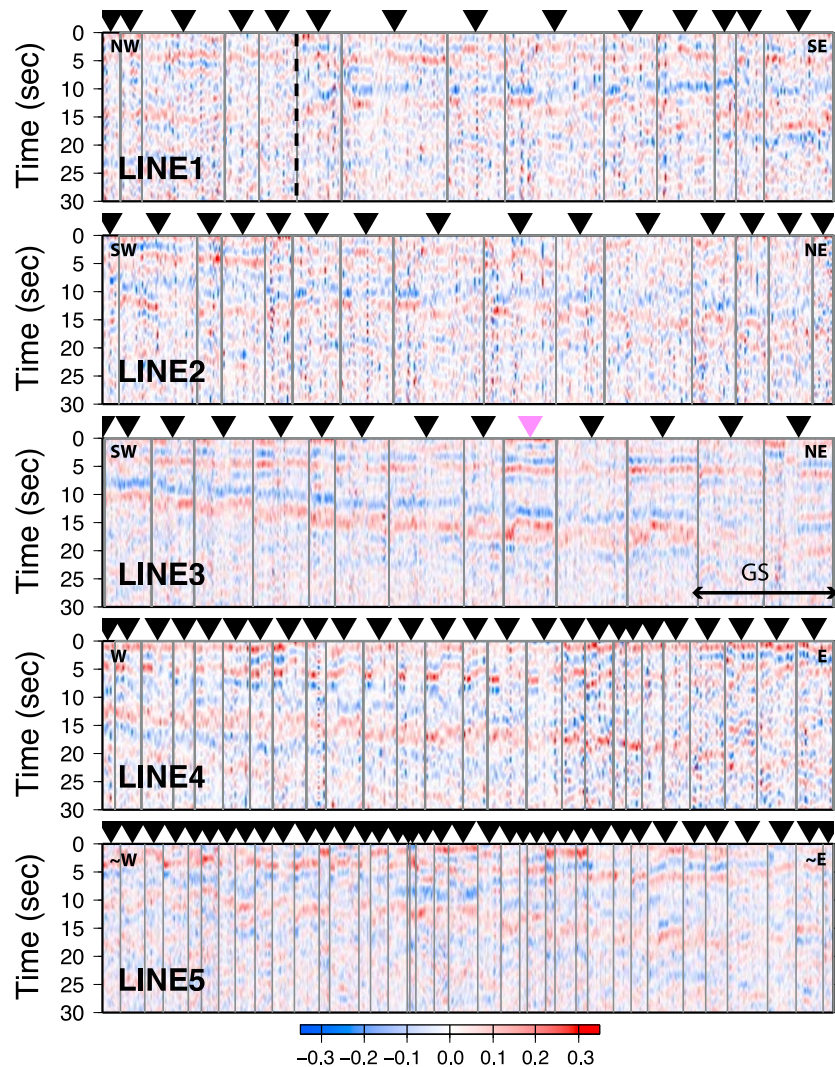


Figure 5. Radial component receiver functions for all data sorted by station position along each line and, for each station, by back azimuth of incident wavefield. Color scale is the same as in Figure 3. The width of each bin, separated by vertical lines and centered on each station along the profile (inverted solid triangles), is commensurate with the number of events used in the analysis. The inverted purple triangle indicates the location of station PGC. Thick vertical black dashed line in line 1 indicates the location where the LVZ signature disappears. The horizontal line labeled GS in line 3 delineates the extent of Georgia Strait. Note that line 5 is a pseudolinear profile based on all data south of 49°N that were organized according to increasing depth of the LVZ beneath each station; geographical directions are thus approximate. These plots demonstrate the existence of the LVZ beneath all stations along the margin.

4.1.1. Line 1

[17] Along line 1 the LVZ is evident beneath stations located to the southeast of the profile, and disappears to the north [Audet *et al.*, 2008]. The seismic response there is more similar to that of a single discontinuity at a typical continental crust-mantle boundary (Moho, $x = m$) with positive P_{mS} and P_{PmS} arrivals at ~ 4 s and ~ 15 s, and a negative P_{SmS} pulse at ~ 22 s.

4.1.2. Line 2

[18] Structural signals along line 2 show evidence of a well-defined LVZ dipping gently NE along the entire profile that is most obvious in the reverberations $P_{P[t,b]S}$ and $P_{S[t,b]S}$ at ~ 10 – 20 s. Oppositely polarized $P_{[t,b]S}$ signals indicate a shallowing of the LVZ signature that is mirrored by earlier

arrivals of reverberated phases and has been interpreted as shearing due to slab stretching in this region [Audet *et al.*, 2008].

4.1.3. Line 3

[19] Data from this line provide the strongest signals from the dipping LVZ [Audet *et al.*, 2009]. All three sets of scattered phases are evident at each station, with amplitudes that diminish downdip beneath the Georgia Strait [Nicholson *et al.*, 2005].

4.1.4. Line 4

[20] Data from this line were used as part of a larger data set in previous studies [Nabelek *et al.*, 1993; Rondenay *et al.*, 2001; Bostock *et al.*, 2002]. The LVZ is evident along the line but with greater variability in phase times, rendering

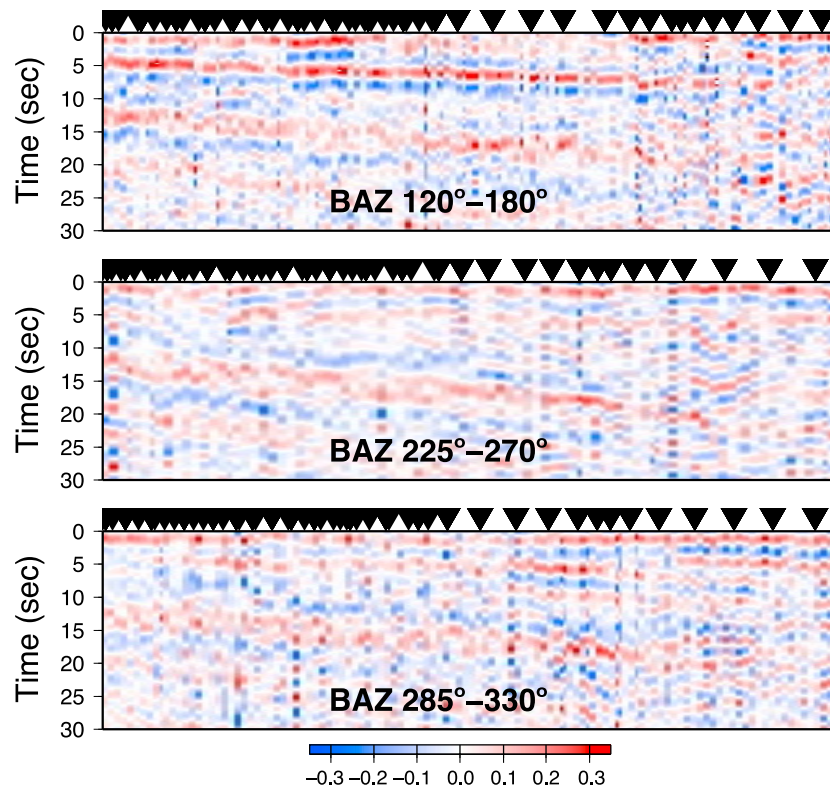


Figure 6. Radial component receiver functions for line 4 sorted as in Figure 5 for three back azimuthal ranges where coverage is densest. Color scale and symbols are the same as in Figure 5.

the plot visually noisy. This distortion is explained by the combined effects of steeper dip of the LVZ, which produces noticeable differences in timing of scattered phases for different back azimuths, and the small number of events recorded at each station. To better visualize coherent structure along line 4, we resorted receiver functions in three back azimuthal ranges (120° – 180° , 225° – 270° , and 285° – 330°) where coverage is densest (Figure 6). Although the data are sparser, the LVZ is clearly seen in all three images, with diminishing signature downdip.

4.1.5. Line 5

[21] In addition to the profiles described above, we organized data from all remaining stations south of the Juan de Fuca strait (from N. Washington to N. California) according to the depth of the LVZ estimated beneath each station (i.e., approximately increasing distance from the trench, indicated by \sim W to \sim E in Figure 5), and plotted them as a pseudolinear profile. P_{xS} phases show some variability, presumably due to structural changes along the margin. Nonetheless, laterally coherent direct conversions and reverberations are visible and provide further evidence for the ubiquity and continuity of LVZ along the entire Cascadia margin.

4.2. Stacking Results Along Dense Linear Arrays

[22] We plotted the depth to top and bottom of slab and V_p/V_S results from stacking receiver functions at individual stations from the four profiles in Figure 7. Horizontal distance is measured from the trench along the trend of each line, except for line 1 where distance is measured from the NW end of the line (Figure 1) with a trend parallel to strike. The results show a dipping LVZ with average vertical

thickness of $\sim 5 \pm 2$ km. The dip along the margin is variable with values ranging between 10° to 20° . The recovered V_p/V_S from the top and bottom of the LVZ indicate that material overlying the LVZ bottom (continental crust + LVZ) has a vertically averaged V_p/V_S that is consistently higher than that overlying the top of LVZ (continental crust alone). This discrepancy suggests that the LVZ has significantly higher V_p/V_S than overlying material, as surmised in section 3. Based on a previous analysis, we interpret high V_p/V_S to arise from elevated pore fluid pressure within the LVZ. In section 5 we explore the nature of the LVZ and discuss its relation with ETS.

5. Nature of LVZ

[23] We can gain insight into the nature of the LVZ by comparing isodepth contours of the top boundary with the slab model of *McCrary et al.* [2006] (Figure 8). We contoured the depth to top of LVZ incorporating results from all stations in the fore arc and using a minimum curvature algorithm [*Wessel and Smith*, 1991] (Figure 9). The 20–40 km contours are in good agreement from northern California to northern Oregon, where a change in dip, strike, and depth of the LVZ is observed. To the north of Oregon, across Washington and southern Vancouver Island, the LVZ deviates from the slab model apparently without loss of continuity. In northern Vancouver Island the LVZ contours are no longer smooth and the layer shallows and disappears toward the northern edge of the slab [*Audet et al.*, 2008], which was interpreted as the signature of slab stretching between the Explorer and Juan de Fuca plates at the northern

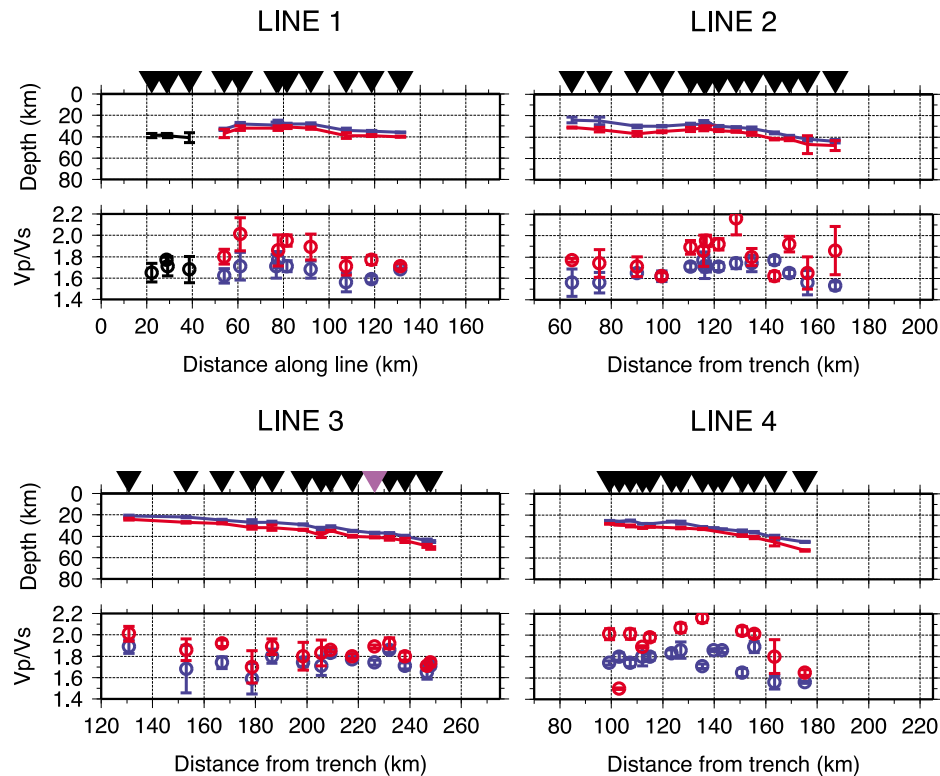


Figure 7. Phase stacking results for individual stations along lines 1–4. Blue and red lines indicate the depth to top and bottom of the LVZ, respectively. Results displayed as black symbols show the locations where LVZ is absent and represent estimates for normal (flat) Moho discontinuity. Note that V_P/V_S for the vertical column overlying the LVZ bottom (in red) is consistently higher than V_P/V_S of the column overlying the top of LVZ (in blue), with a few outliers. Inverted triangles represent the distribution of stations along each line. Inverted purple triangle indicates the location of station PGC along line 3. Distance is measured from the trench along the strike of each line. Distance along line 1 is measured from the NW end of the line.

terminus of Cascadia. We note that the contours drawn from receiver function results are only confidently recovered down to depths of ~ 45 km, beyond which the signal either diminishes or disappears.

[24] To appreciate the significance of these variations in LVZ structure, we must consider the thermal and petrological characteristics of the subduction zone complex, and the water budget of the downgoing slab. Based on the coincidence between the top of LVZ and the slab model in southern Cascadia, it has been postulated that the LVZ corresponds to subducted oceanic crust [Nabelek *et al.*, 1993; Rondenay *et al.*, 2001; Bostock *et al.*, 2002]. The disappearance of the LVZ downdip is explained by the basalt-to-eclogite metamorphic dehydration reaction of oceanic crust at the corresponding pressure and temperature [Nabelek *et al.*, 1993; Rondenay *et al.*, 2001; Bostock *et al.*, 2002]. The water released is then available to partially hydrate and serpentinize the mantle wedge. Both metamorphic reactions (i.e., eclogitization and serpentinization) contribute to reduce the velocity contrast across the top of LVZ, and explain the disappearance of seismic signals. Similar seismic signatures of oceanic crustal eclogitization and fore-arc mantle serpentinization have been reported in other subduction zones, e.g., N-E Japan [Kawakatsu and Watada, 2007], S-W Japan

[Yamauchi *et al.*, 2003; Shiomi *et al.*, 2004] Alaska [Rondenay *et al.*, 2008], Chile [Yuan *et al.*, 2000], Mariana [Tibi *et al.*, 2008], and Greece [Li *et al.*, 2003; Endrun *et al.*, 2004]. In those cases the LVZ coincides with Wadati-Benioff seismicity, consistent with thermal-petrological models of subduction zone metamorphism [Peacock and Wang, 1999]. In Cascadia, however, Wadati-Benioff seismicity is almost absent in Oregon and sparse elsewhere, such that a definitive correspondence between the LVZ and the subducting plate has not been established with certainty.

[25] In northern Cascadia, the LVZ is up to ~ 10 km shallower than the plate interface defined by McCrory *et al.* [2006]. This difference suggests either that the slab is shallower in northern Cascadia than previously thought, or the LVZ is not oceanic crust and the interpretation for southern Cascadia is erroneous [Nicholson *et al.*, 2005]. The conundrum raised here, i.e., whether the LVZ is oceanic crust or not, is a first-order issue in geodynamic modeling of subduction zone processes in Cascadia. To address this problem, we proceed to test the validity of each model by comparing seismological predictions with observations. The set of observations that the correct model must explain include (1) intraslab seismicity, (2) seismic velocity structure, and (3) tremor hypocenters. We will further refer to the slab

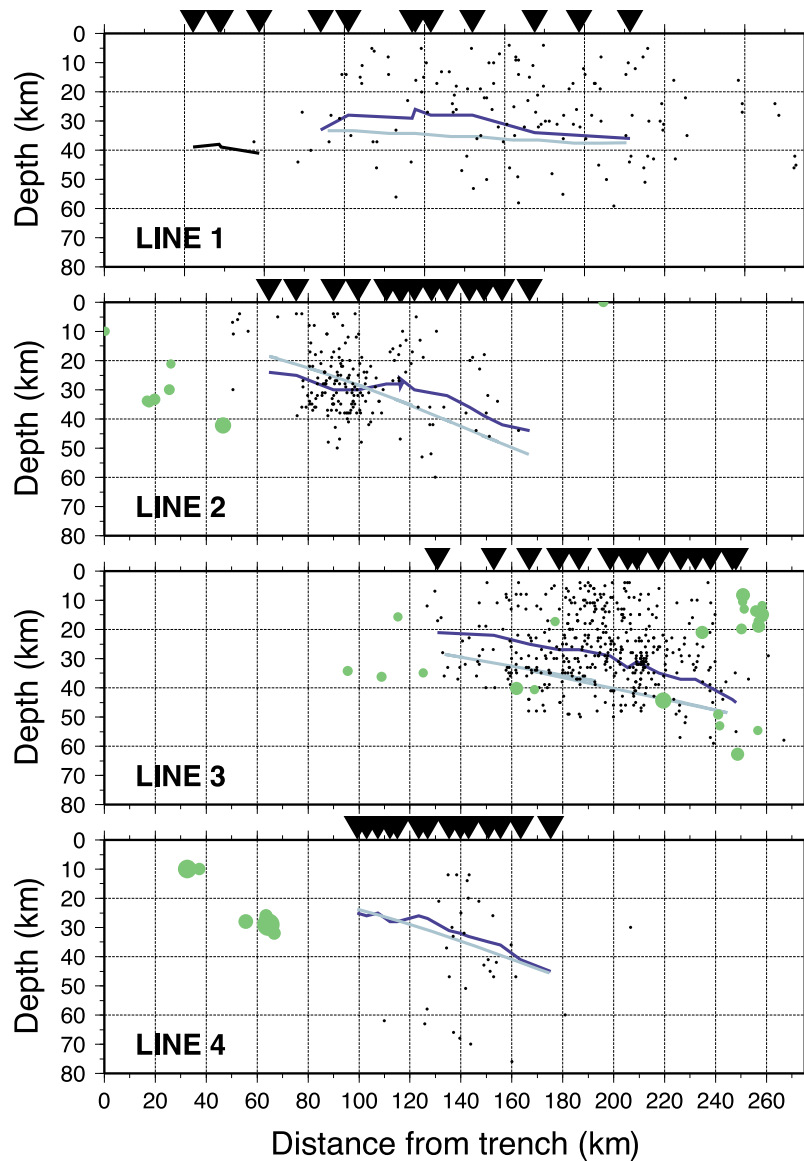


Figure 8. Comparison of the depth to top of LVZ (“shallow slab” model in section 5, dark blue lines) and the top of the plate interface (“deep slab” model in section 5, light blue lines) along the four lines. Superposed on the plots are the earthquake (green dots) and tremor (black dots) hypocenters located within 15 km of the projected lines. Black line indicates estimates for normal Moho discontinuity along line 1.

models based on the compilation by *McCrorry et al.* [2006] and on receiver functions as the “deep slab” and “shallow slab” models, respectively.

5.1. Intraslab Earthquakes

[26] Intraslab earthquake activity at intermediate depth (50–200 km) manifests internal deformation of subducting lithosphere as inclined zones of earthquake occurrence from the trench to upper mantle depths [*Kirby et al.*, 1996]. Double Wadati-Benioff zones, i.e., parallel planes of seismicity, are a quasi-ubiquitous feature of subduction zones [*Brudzinski et al.*, 2007], the exception being Cascadia where intermediate-depth intraslab seismicity is unusually sparse. A shallow (15–25 km depth) double seismic zone has been found at the southern end of Cascadia within the Gorda plate [*Wang and Rogers*, 1994], and precisely re-

located intraslab earthquakes in northern Cascadia reveal the localized occurrence of an intermittent, shallow (40–62 km depth) double seismic zone separated by only 2–3 km [*Cassidy and Waldhauser*, 2003].

[27] Intraslab earthquakes are unlikely to occur by ordinary brittle fracture and frictional failure due to the large confining pressure in the slab and thus require a weakening (embrittlement) mechanism [*Kirby et al.*, 1996]. While a number of mechanisms have been proposed to explain the origin of the Cascadia double seismic zones (e.g., upper and lower bending fiber of a flexing plate [e.g., *Wang et al.*, 2004b]; thermally controlled, layered rheology [*Wang and Rogers*, 1994]), thermal-petrological models of subduction zone metamorphism successfully predict the locations of intraslab earthquakes based on dehydration embrittlement by the breakdown of hydrous mineral phases that release

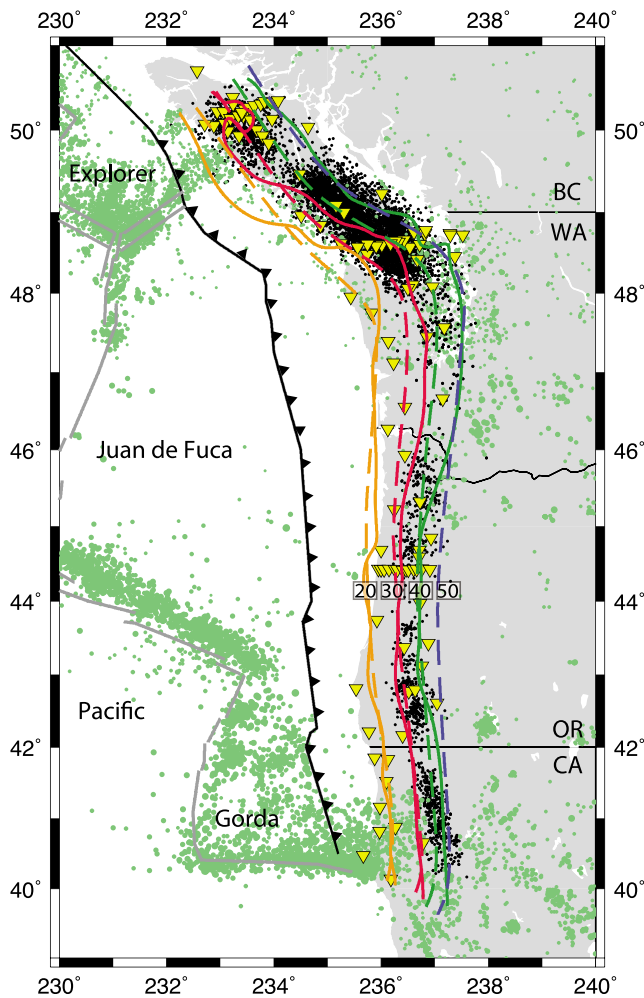


Figure 9. Depths contours of the top of LVZ (“shallow slab” model in section 5, solid lines) and the top of the plate interface (“deep slab” model in section 5, dashed lines) along the Cascadia margin. Earthquake epicenters from the GSC and USGS catalogues for $M > 2$ are shown as green dots; tremor epicenters appear as black dots. Broadband stations used in the analysis are displayed as inverted yellow triangles. Numbers indicate depth (in km) to each contour. Solid black line with arrowheads indicates the location of the trench offshore.

fluids and increase pore fluid pressure [Kirby *et al.*, 1996; Hacker *et al.*, 2003]. Such prograde metamorphic reactions also increase rock density and produce a negative volume change that may help trigger hydrofracturing [Hacker *et al.*, 2003]. Dehydration embrittlement is controlled by pressure and temperature (P-T) conditions and the water budget of the downgoing slab. The most likely petrologic candidates for dehydration embrittlement in the upper plane of double Wadati-Benioff zones are hydrated metabasalts. The lower plane is typically explained by antigorite and/or chlorite dehydration reactions [Peacock, 2001; Brudzinski *et al.*, 2007].

[28] In a warm subduction zone such as Cascadia, pressure and temperature (P-T) conditions within the oceanic crust predict the last major dehydration reaction for meta-

basalts, i.e., eclogitization, to occur at nearly constant pressure, independent of temperature, whereas the serpentine dehydration reaction occurs at nearly constant temperature, independent of pressure (along the 600°C isotherm) [Preston *et al.*, 2003]. Consequently, eclogitization should occur at a roughly constant depth interval within the slab crust, whereas deserpentinization should follow the 600°C isotherm within the slab mantle. Since P-T conditions within the plate are inferred on the basis of observed heat flux and assumed plate geometry, one might expect the two plate models for northern Cascadia to predict different patterns of intraslab seismicity.

[29] As mentioned above, precisely relocated intraslab earthquakes in northern Cascadia locally cluster within two parallel bands of shallow seismic activity separated by 2–3 km, at depths of 40–60 km, upon which they merge into one seismic zone and taper out horizontally at ~60 km [Cassidy and Waldhauser, 2003]. We note that about 12%–15% of small magnitude ($M < 3$) events are located above the slab surface as defined by the deep slab model [Wang *et al.*, 2004a], mostly at depths of 55–65 km [Cassidy and Waldhauser, 2003]. In a separate study in the Puget Sound region, Preston *et al.* [2003] located intraslab earthquakes within a single, dipping plane of relatively uniform seismicity at depths of 30–70 km.

[30] In the deep slab model, the maximum depth of intraslab crustal earthquakes is constrained to the depth to the basalt-to-eclogite dehydration reaction predicted at ~50 km [Peacock and Wang, 1999]. Shallow intraslab mantle earthquakes due to serpentine dehydration would occur along the 600°C isotherm, which lies just below the oceanic Moho [Preston *et al.*, 2003]. Thus, based on the deep slab model, intraslab earthquakes are predicted to occur within or immediately below the oceanic Moho.

[31] In the shallow slab model, temperatures at any point in the slab will be depressed to satisfy heat flux constraints, and may therefore cause a shift to lower-grade metamorphic facies. However, because eclogitization at these temperatures occurs at roughly constant pressure, the maximum depth for intraslab crustal earthquakes remains ~50 km. In contrast, the predicted serpentine dehydration reaction will now occur well below the oceanic Moho, as the 600°C isotherm moves well into the slab mantle. Thus, based on the shallow slab model, intraslab seismicity is predicted to occur both within the oceanic crust at ~50 km depth, and within the slab mantle some ~10 km below and subparallel to the Moho. Such predictions are generally consistent with observations of downdip tapering of intraslab seismicity at ~50–60 km [Cassidy and Waldhauser, 2003], and updip intraslab seismicity occurring within the slab mantle (Figure 8) [Preston *et al.*, 2003; Nicholson *et al.*, 2005; Abers *et al.*, 2009].

[32] In summary, observations of intraslab seismicity and predictions made on the basis of simple thermal-petrological models of subduction metamorphism cannot rule out either of the two slab models.

5.2. Seismic Velocity Structure

[33] 3-D regional seismic structure derived from active source and earthquake tomographic models provide bulk information on mineralogical and thermal properties of the subduction complex. In Cascadia a variety of models

obtained using different data sets and inversion parameters, and possessing different spatial resolution investigate subducting slab structure [e.g., *Ramachandran et al.*, 2006, and references therein]. In a recent model, *Ramachandran et al.* [2006] employed a joint inversion of active source and earthquake data to image the Juan de Fuca slab and fore-arc structure beneath southwest British Columbia and northwest Washington. The 7.6 km/s isovelocity contour was taken as a proxy for the oceanic Moho, and the top of the Juan de Fuca plate was represented as a smooth surface 7 km above.

[34] Their tomographic model is characterized by a broad zone of low P velocities (6.4–6.6 km/s) lying above and downdip of the inferred megathrust locked zone, that coincides with the E layer. This feature has been interpreted as a band of fluid-filled lenses with 1%–4% saline water porosity within the overriding crust on the basis of seismic velocity models, intraslab seismicity, and reflection profiles offshore [*Hyndman*, 1988, and references therein]. The interpretation requires upward migration of fluids from the dehydrating slab into the overlying fore-arc crust. Reduced temperature causes retrograde metamorphic reactions and mineral precipitation which in turn create an impermeable barrier at midcrustal depths.

[35] In receiver function images, prominent converted signals originate from a LVZ coincident with the E layer, without any obvious signature of deeper structures. In a previous study, *Nicholson et al.* [2005] concluded that the teleseismic signature of the E layer manifests an overall S velocity reduction within the oceanic crust due to the presence of free water. In this interpretation the E reflectors are generated by highly localized zones of water saturation, leading to the formation of thin dipping, fluid-filled lenses of high porosity within the oceanic crust, producing the high reflectivity.

[36] In both interpretations the presence of water is necessary to account for the high reflectivity of the E layer, its high conductivity, low density, and low P and S velocities. Observations of V_p/V_s (or the equivalent Poisson's ratio) made by stacking receiver functions reveal that V_p/V_s of the LVZ is significantly higher than that of the overlying material (Figure 7), a result confirmed by the detailed analysis of Poisson's ratio beneath line 3 [*Audet et al.*, 2009]. High Poisson's ratio within the LVZ favors elevated pore fluid pressure and implies an impermeable boundary at the top of the LVZ, consistent with observations of velocity contrasts at this boundary [*Audet et al.*, 2009].

[37] Elevated pore fluid pressure within and below the LVZ provides a means to reconcile the low-resolution tomographic model with a shallow plate interface as it not only increases Poisson's ratio but also depresses absolute velocities dramatically (up to 20% and 30% for P and S , respectively, in the measurements of *Christensen* [1996]). A commensurate reduction in the value of isovelocity contour chosen as proxy for oceanic Moho would certainly suffice to elevate the top of plate to the level predicted in the shallow slab model.

5.3. Tremor Hypocenters

[38] Nonvolcanic tremor belongs to a different class of seismicity than normal earthquakes [*Ide et al.*, 2007a, 2008], and its triggering mechanism is not well understood. In S-W Japan, tremor hypocenters are located within a relatively

narrow depth band, in the vicinity of the mantle wedge corner, and moment tensor solutions suggest that tremor is caused by propagating, slow shear slip on the plate interface [*Shelly et al.*, 2006, 2007a; *Ide et al.*, 2007b]. Moreover, Wadati-Benioff seismicity lies definitively below the zone of ETS occurrence, straddling the inferred oceanic crustal Moho. In Cascadia, however, tremor hypocenters are not so well constrained, and such a correspondence has not been clearly established. Nonetheless, the unique spatial characteristics of tremor occurrence can be used to discriminate between the two slab models, provided that the mechanism of tremor in southwest Japan also applies in Cascadia. Given the similarity in subduction zone structure between southwest Japan and Cascadia, this assumption is reasonably justified.

[39] The first test that we can perform concerns the epicentral distribution of tremors with respect to slab contours. If, as observed in Japan, tremor occurs along the plate interface, then the slab model that produces the most narrow tremor distribution in depth should be preferred. We proceed by compiling tremor epicenters along the Cascadia margin within three different segments: (1) Vancouver Island, (2) Washington, and (3) Oregon and northern California (Figure 9). Data from Vancouver Island span ~10 years of seismic instrumentation and provide the densest coverage of tremor determination [*Kao et al.*, 2009]. Data from Washington span 3 ETS events from 2002 to 2005 [*McCausland et al.*, 2005]. Data from Oregon and northern California were obtained from 3 ETS events between 2005 and 2007 [*Boyarko and Brudzinski*, 2010]. We then calculate the percentage of tremor epicenters falling within 2.5 km bins of slab depth contours for each of the two slab models, to determine which model provides the narrowest depth range of tremor occurrence, in accordance with results from southwest Japan.

[40] Histograms of tremor occurrence versus isodepth slab contours are presented in Figure 10. Histograms for the shallow slab model produce narrow normal-like distributions and peak at 35 km depth for each of the three segments. This relatively narrow distribution suggests that tremor bursts accompanying slow slip presumably occur near the intersection of the plate interface with the Moho of the overlying lithosphere. In contrast, histograms for the deep slab model imply that tremor epicenters do not follow isodepth contours across Vancouver Island, as evidenced by the wider, asymmetric distribution, and that tremor can occur where oceanic crust has already penetrated well into the mantle (>40 km). Although errors in both slab models and in epicenter determinations may affect the result, the narrow distribution of tremor around the shallow slab contours suggests that those estimates are accurate; otherwise we would not expect clustering around specific slab contours for any slab model. Provided that tremor preferentially occurs on the plate interface near but updip of the mantle wedge corner, these results indicate that the shallow slab model is a better candidate to explain the locations of tremor epicenters. Furthermore, it better reproduces the spatial relation between tremor location, Wadati-Benioff seismicity and LVZ that has been documented in southwest Japan.

[41] Tremor hypocenter locations and the few precisely determined low-frequency earthquake hypocenters can also be used to address the depth to the plate interface. The recent

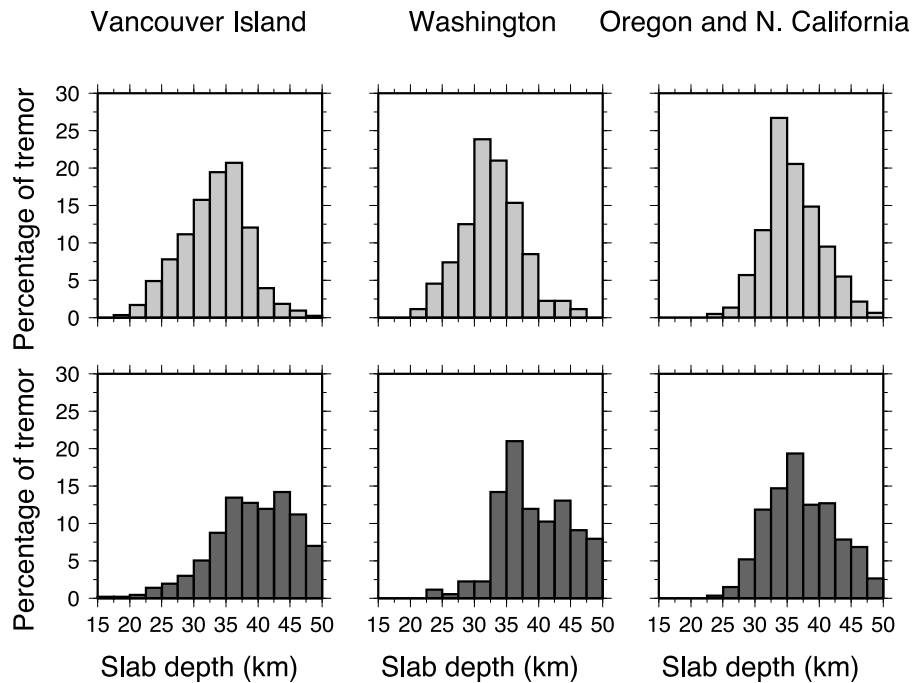


Figure 10. Histograms of tremor epicenter distribution within 2.5 km depth contours based on the (top) shallow and (bottom) deep slab models. Histograms for the shallow slab model reveal normal-like distributions peaking at ~ 35 km. Histograms for the deep slab model are flatter and do not show tremor focusing along specific slab depth contours.

compilation by *Kao et al.* [2009] for Vancouver Island shows that the highest concentration of tremor activity occurs at depths of 25–35 km, in agreement with studies in central and southern Cascadia [*McCausland et al.*, 2005], and centers on the E layer. *Kao et al.* [2009] also show that a set of clearly identified low-frequency earthquakes occurring during a tremor sequence were generated on the E layer, and all exhibit reverse thrust-fault slip mechanisms. Moreover, *Wech and Creager* [2007] demonstrate that horizontal particle motions of tremor-generated *S* waves are in the direction of plate convergence, an indication that they are caused by propagating slow shear slip on the plate interface, as in Japan.

[42] These observations put the deep slab model at odds with expectations of fault behavior. Indeed, repeated slip on a fault at very low stress drops implies that it is a significant zone of weakness. Thus, if the plate interface defined by the top of oceanic crust is stronger than parallel, dipping faults lying 10 km shallower, slip deficiency will be preferentially accommodated at the shallower interface, thereby defining the new plate boundary. This situation requires that a shear zone be created within the overriding lithosphere by retrograde metamorphic reactions associated with percolating fluids trapped at a dipping impermeable interface above the plate boundary [*Hyndman*, 1988]. Alternatively, it would appear far simpler to explain reverse slip on the E layer if the LVZ is subducted oceanic crust.

6. Relation With ETS

[43] A number of observations suggests that subduction zone structure exerts a fundamental control over ETS occurrence and recurrence. In general, ETS events seem to occur

preferentially in young (warm) subduction zones, where the slab dips shallowly, and thus where there is most contact with the crust of the overriding lithosphere. Young subducting plates also offer more resistance to subduction, and are likely to dehydrate at shallower levels than older subduction zones. ETS in Alaska appears to contradict this trend because the subducting Pacific plate is old and dips steeply; however, the underthrusting Yakutat block is unusually thick and affords more resistance to subduction. In Chile, ETS may (or may not) be related to flat slab subduction. In this section we examine the relation between subduction zone fore-arc structure and ETS.

6.1. ETS and Downgoing Plate Structure

[44] To understand the relation between subducting plate structure and the occurrence of ETS in Cascadia, it is useful to describe similar observations in southwest Japan, where dense seismic and geodetic instrumentation have allowed accurate characterization of structure, tremor hypocenters, and slow slip events. *Obara* [2002] first noted that tremor associated with subduction occurred on average at a depth of 30 km, in the vicinity of the Moho discontinuity, an observation further refined by *Katsumata and Kamaya* [2003]. He also reported the spatial coincidence between tremor and slow slip events [*Obara et al.*, 2004]. Subsequently, *Shelly et al.* [2006] demonstrated that precisely relocated low-frequency earthquakes originating during tremor sequences occurred on the plate interface, within the frictional stability transition region between the updip seismic and downdip aseismic zone, and where the megathrust fault is in contact with the crust of the overlying plate.

[45] In Cascadia, despite the initial recognition of concurrent slow slip and tremors forming ETS events [Rogers and Dragert, 2003], a clear relation between plate structure and tremor locations has remained elusive. As we demonstrated in section 5, tremor epicenters are consistent with an origin close to the Moho discontinuity of the continental plate within a depth range of 25–40 km. This region also coincides with the inferred zone of slow slip [Dragert et al., 2001; Szeliga et al., 2008], and may define the depth to the intersection of the slab with continental Moho in the Cascadia fore arc. The new plate model in northern Cascadia implies that the thermally controlled extent of locking on the plate interface may have to be revised landward, bringing the updip limit of tremor closer to the locked zone. This downdip adjustment of the locked zone and the occurrence of ETS at the edge of the megathrust earthquake source is consistent with observations in southwest Japan [Ide et al., 2007a], and possibly indicates a link with the downdip extent of future rupture [Szeliga et al., 2008].

6.2. Conceptual Model

[46] Proposed mechanisms for the triggering of ETS events are based on several observations: (1) slow slip events show a direction of motion reverse to plate convergence that can be explained by slip on the plate interface [Dragert et al., 2001], (2) focal mechanisms of low-frequency earthquakes and tremors accompanying slow slip suggest low-angle thrust motion on the plate interface [Shelly et al., 2006; Ide et al., 2007b], and (3) tidal modulation of tremors [Rubinstein et al., 2007a] and triggering by distant earthquakes [Rubinstein et al., 2007b] indicate very low stress drops.

[47] Tremor and slow slip occurring on the plate interface and triggered at very low dynamic stresses imply very low effective stress on the megathrust within the frictional stability transition zone, presumably due to elevated pore fluid pressure, consistent with observations of high V_P/V_S within the subducted oceanic crust in Japan and Cascadia [Shelly et al., 2006; Wang et al., 2006; Audet et al., 2009], with fluids provided by dehydration of the subducting slab. The large spatial dimension and short recurrence of slow slip also requires near-lithostatic pore pressure in rate-and-state friction models [Liu and Rice, 2005, 2007], consistent with conditions for the onset of low-pressure metamorphic dehydration reactions [Fyfe et al., 1978]. Near-lithostatic pore fluid pressure implies a low-permeability plate boundary, where the sealing agents can be a combination of grain size reduction on the fault [Caine et al., 1996] possibly caused by shattering of upper crust [Wang et al., 2004a], and the precipitation of minerals during fluid flow [Kato et al., 2003; Meneghini and Moore, 2007].

[48] The relations between slow slip, tremor, and fluids may provide clues into the generation of ETS. While several mechanisms have been proposed (see Schwartz and Rokosky [2007] for a summary), we emphasize here the potential influence of structure based on a range of observations: (1) the narrow occurrence of tremors and slow slip events along the plate interface near the depth to the last major dehydration reaction (i.e., eclogitization) of metabasalts within subducting oceanic crust in warm slabs, (2) fluids released from the slab are available to partially serpentinize the mantle wedge downdip, and (3) the implied transition in

permeability coincides with the frictional stability transition zone [Audet et al., 2009].

[49] Based on this evidence, we propose a conceptual model for the generation of ETS that bridges the gap between models of spatial occurrence and recurrence intervals of ETS and is consistent with available observations. In this model ETS is explained by a sequence of events involving feedback processes: (1) dehydration of the subducting oceanic crust releases fluids that are subsequently trapped at the plate boundary with overriding crust but released upon entry into the mantle wedge; (2) trapped fluids contribute to build overpressure within the oceanic crust at shallow levels and lower the effective stress on the plate boundary; (3) at near-lithostatic pore fluid pressure the effective stress is low enough to allow triggered slip at small dynamic stresses; (4) propagating slip and hydrofracturing of the seal increase permeability and trigger fluid flow into the overriding plate or along the plate interface, producing a positive feedback and enhancing the propagation of slow slip and tremor; and (5) the pumping of fluids decreases the pore fluid pressure and produces a negative feedback, increasing the effective stress and stopping the reverse slip motion.

[50] This model accounts for the dynamic triggering of tremor by distant earthquakes at very low stress drops, the predominance of ETS in warm subduction zones where slab temperatures are higher and dehydration occurs at shallow levels, and episodicity of ETS due to pore fluid pressure buildup and release. The variable frequency of ETS recurrence can then be explained by different rates of slab dehydration, permeability and rheology of the upper plate, variable lithostatic pressure at the depth corresponding to the transition zone, or a combination of these factors [Brudzinski and Allen, 2007]. Diffusion of excess pore pressure can also potentially explain the migration characteristics of ETS along the margin [Kao et al., 2007; Shelly et al., 2007b]. This model is consistent with rate-and-state friction models [Liu and Rice, 2005; Wang et al., 2006; Liu and Rice, 2007], but also incorporates the effects of permeability enhancement [Elkhoury et al., 2006] by crustal densification and/or volume change during eclogitization, promoting fluid flow and slip. It is also consistent with dynamically triggered tremor generated by permeability increase involving pore dilatation in fractured media at high pore fluid pressure and subsequent fluid flow [Elkhoury et al., 2006; Miyazawa and Mori, 2006; Miyazawa and Brodsky, 2008].

[51] This model does not address several key components of the ETS process; for example the nearly complete release of inter-ETS strain accumulation during slow slip. We expect more definitive insights into the behavior of episodic pore pressure buildup from numerical models that incorporate poroelastic effects.

7. Conclusion

[52] This paper presents seismic receiver function results from a margin-wide study of subsurface discontinuities beneath the Cascadia fore-arc crust. We find ubiquitous evidence for a low-velocity zone from northern California to northern Vancouver Island that we identify as subducted oceanic crust on the basis of intraslab seismicity, seismic velocity structure, and occurrence of nonvolcanic tremor,

consistent with thermal-petrological models of the Cascadia subduction zone structure. This result requires a revision to the Cascadia slab model, particularly in northern Cascadia. We relate the occurrence of ETS to the major structural elements and find that (1) nonvolcanic tremor occurs where slab depth is 30–40 km; (2) the peak occurrence of tremors roughly coincides with the intersection of the plate interface with the overlying continental crust-mantle boundary (i.e., the mantle wedge corner); and (3) tremors occur within the frictional stability transition zone, where permeability changes and water release from prograde metamorphic reactions is expected. Based on these findings, we propose a conceptual model for the generation of ETS where the occurrence and recurrence of slow slip and low-frequency tremor are explained by episodic pore pressure buildup due to dehydration of oceanic crust, which releases fluids that are trapped at the low-permeability plate interface. At near-lithostatic pore fluid pressure, tremor and slip are triggered by hydrofracturing of the plate boundary seal and fluids are pumped from the downgoing crust. Precipitation sealing of the plate interface or grain size reduction due to fracture eventually restores the low permeability, and the cycle resumes. Recurrence intervals and migration characteristics of ETS along the margin can be explained by pore fluid pressure diffusion and mechanical properties of the upper plate.

[53] **Acknowledgments.** We are grateful to H. Kao and W. McCausland for providing us with tremor locations for Vancouver Island and Washington. This paper was much improved by comments from the Associate Editor and two reviewers. We acknowledge discussions with E. Davis, S. Peacock, and N. Christensen. This work was partially funded by the Miller Institute for Basic Research in Science (UC Berkeley) through a Fellowship to P.A., the Natural Science and Engineering Research Council (Canada), and the National Science Foundation. Data are made available by the Canadian National Data Center (CNDC) and the IRIS consortium.

References

- Abers, G. A. (2005), Seismic low-velocity layer at the top of subducting slabs beneath volcanic arcs: Observations, predictions, and systematics, *Phys. Earth Planet. Inter.*, *149*, 7–29, doi:10.1016/j.pepi.2004.10.002.
- Abers, G. A., L. S. MacKenzie, S. Rondenay, Z. Zhang, A. G. Wech, and K. C. Creager (2009), Imaging the source region of Cascadia tremor and intermediate-depth earthquakes, *Geology*, *37*, 1119–1122, doi:10.1130/G30143A.1.
- Audet, P., M. G. Bostock, J.-P. Mercier, and J. F. Cassidy (2008), Morphology of the Explorer/Juan de Fuca slab edge in northern Cascadia: Imaging plate capture at a ridge-trench-transform triple junction, *Geology*, *36*, 895–898, doi:10.1130/G25356.
- Audet, P., M. G. Bostock, N. I. Christensen, and S. M. Peacock (2009), Seismic evidence for overpressured subducted oceanic crust and megathrust fault sealing, *Nature*, *457*, 76–78, doi:10.1038/nature07650.
- Bostock, M. G. (1998), Mantle stratigraphy and evolution of the Slave province, *J. Geophys. Res.*, *103*, 21,183–21,200.
- Bostock, M. G., R. D. Hyndman, S. Rondenay, and S. M. Peacock (2002), An inverted continental Moho and serpentinization of the forearc mantle, *Nature*, *417*, 536–539.
- Boyarko, D. C., and M. R. Brudzinski (2010), Spatial and temporal patterns of nonvolcanic tremor along the southern Cascadia subduction zone, *J. Geophys. Res.*, doi:10.1029/2008JB006064, in press.
- Brudzinski, M. R., and R. M. Allen (2007), Segmentation in episodic tremor and slip all along Cascadia, *Geology*, *35*, 907–910, doi:10.1130/G23740A.1.
- Brudzinski, M. R., C. H. Thurber, B. R. Hacker, and E. R. Engdahl (2007), Global prevalence of double Benioff zones, *Science*, *316*, 1472–1474.
- Caine, J. S., J. P. Evans, and C. B. Foster (1996), Fault zone architecture and permeability structure, *Geology*, *24*, 1025–1028.
- Cassidy, J. F., and R. M. Ellis (1993), S-wave velocity structure of the northern Cascadia subduction zone, *J. Geophys. Res.*, *98*, 4407–4421.
- Cassidy, J. F., and F. Waldhauser (2003), Evidence for both crustal and mantle earthquakes in the subducting Juan de Fuca plate, *Geophys. Res. Lett.*, *30*(2), 1095, doi:10.1029/2002GL015511.
- Cassidy, J. F., R. M. Ellis, C. Karavas, and G. C. Rogers (1998), The northern limit of the subducted Juan de Fuca plate system, *J. Geophys. Res.*, *103*, 26,949–26,961.
- Christensen, N. I. (1996), Poisson's ratio and crustal seismology, *J. Geophys. Res.*, *101*, 3139–3156.
- Clowes, R. M., R. M. Ellis, Z. Hajnal, and I. F. Jones (1983), Seismic reflections from subducting lithosphere?, *Nature*, *303*, 668–670.
- Dragert, H., K. Wang, and T. S. James (2001), A silent slip event on the deeper Cascadia subduction interface, *Science*, *292*, 1525–1528.
- Elkhoury, J. E., E. E. Brodsky, and D. Agnew (2006), Seismic waves increase permeability, *Nature*, *441*, 1135–1138.
- Endrun, B., T. Meier, M. Bischoff, and H.-P. Harjes (2004), Lithospheric structure in the area of Crete constrained by receiver functions and dispersion analysis of Rayleigh phase velocities, *Geophys. J. Int.*, *158*, 592–608.
- Ferris, A., G. A. Abers, D. H. Christensen, and E. Veenstra (2003), High resolution image of the subducted Pacific (?) plate beneath central Alaska, 50–150 km depth, *Earth Planet. Sci. Lett.*, *214*, 575–588.
- Frederiksen, A. W., and M. G. Bostock (2000), Modelling teleseismic waves in dipping anisotropic structures, *Geophys. J. Int.*, *141*, 401–412.
- Fyfe, W. S., N. J. Price, and A. B. Thomson (1978), *Fluids in the Earth's Crust*, Elsevier, Amsterdam.
- Green, A. G., R. M. Clowes, C. J. Yorath, C. Spencer, E. R. Kanasewich, M. T. Brandon, and A. S. Brown (1986), Seismic reflection imaging of the subducting Juan de Fuca plate, *Nature*, *319*, 210–213.
- Hacker, B. R., S. M. Peacock, G. A. Abers, and S. D. Holloway (2003), Subduction factory: 2. Are intermediate-depth earthquakes in subducting slabs linked to metamorphic dehydration reactions?, *J. Geophys. Res.*, *108*(B1), 2030, doi:10.1029/2001JB001129.
- Hyndman, R. D. (1988), Dipping seismic reflectors, electrically conductive zones, and trapped water in the crust over a subducting plate, *J. Geophys. Res.*, *93*, 13,391–13,405.
- Ide, S., G. C. Beroza, D. R. Shelly, and T. Uchide (2007a), A scaling law for slow earthquakes, *Nature*, *447*, 76–79.
- Ide, S., D. R. Shelly, and G. C. Beroza (2007b), Mechanism of deep low frequency earthquakes: Further evidence that deep non-volcanic tremor is generated by shear slip on the plate interface, *Geophys. Res. Lett.*, *34*, L03308, doi:10.1029/2006GL028890.
- Ide, S., K. Imanishi, Y. Yoshida, G. C. Beroza, and D. R. Shelly (2008), Bridging the gap between seismically and geodetically detected slow earthquakes, *Geophys. Res. Lett.*, *35*, L10305, doi:10.1029/2008GL034014.
- Kao, H., and S.-J. Shan (2004), The Source-Scanning Algorithm: Mapping the distribution of seismic sources in time and space, *Geophys. J. Int.*, *157*, 589–594, 10.1111/j.1365-246X.2004.02276.x.
- Kao, H., S.-J. Shan, H. Dragert, G. Rogers, J. F. Cassidy, and K. Ramachandran (2005), A wide depth distribution of seismic tremors along the northern Cascadia margin, *Nature*, *436*, 841–844.
- Kao, H., S.-J. Shan, G. Rogers, and H. Dragert (2007), Migration characteristics of seismic tremors in the northern Cascadia margin, *Geophys. Res. Lett.*, *34*, L03304, doi:10.1029/2006GL028430.
- Kao, H., S.-J. Shan, H. Dragert, and G. Rogers (2009), Northern Cascadia episodic tremor and slip: A decade of tremor observations from 1997 to 2007, *J. Geophys. Res.*, *114*, B00A12, doi:10.1029/2008JB006046.
- Kato, A., A. Sakaguchi, S. Yoshida, and H. Mochizuki (2003), Permeability measurements and precipitation sealing of basalt in an ancient exhumed fault of a subduction zone, *Bull. Earthquake Res. Inst. Univ. Tokyo*, *78*, 83–89.
- Katsumata, A., and N. Kamaya (2003), Low-frequency continuous tremor around the Moho discontinuity away from volcanoes in the southwest Japan, *Geophys. Res. Lett.*, *30*(1), 1020, doi:10.1029/2002GL015981.
- Kawakatsu, H., and S. Watada (2007), Seismic evidence for deep-water transportation in the mantle, *Science*, *316*, 1468–1471.
- Kirby, S. H., E. R. Engdahl, and R. Denlinger (1996), Intermediate-depth intraslab earthquakes and arc volcanism as physical expressions of crustal and uppermost mantle metamorphism in subducting slabs (overview), in *Subduction: Top to Bottom*, *Geophys. Monogr. Ser.*, vol. 96, edited by G. E. Bebout et al., pp. 195–214, AGU, Washington, D. C.
- Kodaira, S., T. Iidaka, A. Kato, J.-O. Park, T. Iwasaki, and Y. Kaneda (2004), High pore fluid pressure may cause silent slip in the Nankai Trough, *Science*, *304*, 1295–1298.
- Kurtz, R. D., J. M. DeLaurier, and J. C. Gupta (1986), A magnetotelluric sounding across Vancouver Island detects the subducting Juan de Fuca plate, *Nature*, *321*, 596–599.
- Li, X., G. Bock, A. Vafidis, R. Kind, H.-P. Harjes, W. Hanka, K. Wylegalla, M. van der Meijde, and X. Yuan (2003), Receiver function study of the

- Hellenic subduction zone: Imaging crustal thickness variations and the oceanic Moho of the descending African lithosphere, *Geophys. J. Int.*, *155*, 733–748.
- Liu, Y., and J. R. Rice (2005), Aseismic slip transients emerge spontaneously in three-dimensional rate and state modeling of subduction earthquake sequences, *J. Geophys. Res.*, *110*, B08307, doi:10.1029/2004JB003424.
- Liu, Y., and J. R. Rice (2007), Spontaneous and triggered aseismic deformation transients in a subduction fault model, *J. Geophys. Res.*, *112*, B09404, doi:10.1029/2007JB004930.
- McCausland, W., S. Malone, and D. Johnson (2005), Temporal and spatial occurrence of deep non-volcanic tremor: From Washington to northern California, *Geophys. Res. Lett.*, *32*, L24311, doi:10.1029/2005GL024349.
- McCrory, P. A., J. L. Blair, and D. H. Oppenheimer (2006), Depth to the Juan de Fuca slab beneath the Cascadia subduction margin—A 3-D model for sorting earthquakes, *U.S. Geol. Surv. Data Ser.*, *91*, U.S. Geol. Surv., Reston, Va. (Available at <http://pubs.usgs.gov/ds/91/>)
- Meneghini, F., and J. C. Moore (2007), Deformation and hydrofracturing in a subduction thrust at seismogenic depths: The Rodeo Cove thrust zone, Marin Headlands, California, *Geol. Soc. Am. Bull.*, *119*, 174–183.
- Mercier, J.-P., M. G. Bostock, P. Audet, J. B. Gaherty, E. J. Garnero, and J. Revenaugh (2008), The teleseismic signature of fossil subduction: Northwestern Canada, *J. Geophys. Res.*, *113*, B04308, doi:10.1029/2007JB005127.
- Miyazawa, M., and E. E. Brodsky (2008), Deep low-frequency tremor that correlates with passing surface waves, *J. Geophys. Res.*, *113*, B01307, doi:10.1029/2006JB004890.
- Miyazawa, M., and J. Mori (2006), Evidence suggesting fluid flow beneath Japan due to periodic seismic triggering from the 2004 Sumatra-Andaman earthquake, *Geophys. Res. Lett.*, *33*, L05303, doi:10.1029/2005GL025087.
- Nabelek, J., X.-Q. Li, S. Azevedo, J. Braunmiller, A. Fabritius, B. Leitner, A. Trehu, and G. Zandt (1993), A high-resolution image of the Cascadia subduction zone from teleseismic converted phases recorded by a broadband seismic array, *Eos Trans. AGU*, *74*(43), Fall Meet. Suppl., 431.
- Nicholson, T., M. G. Bostock, and J. F. Cassidy (2005), New constraints on subduction zone structure in northern Cascadia, *Geophys. J. Int.*, *161*, 849–859.
- Obara, K. (2002), Nonvolcanic deep tremor associated with subduction in southwest Japan, *Science*, *296*, 1679–1681.
- Obara, K., H. Hirose, F. Yamamizu, and K. Kasahara (2004), Episodic slow slip events accompanied by non-volcanic tremors in southwest Japan subduction zone, *Geophys. Res. Lett.*, *31*, L23602, doi:10.1029/2004GL020848.
- Peacock, S. M. (2001), Are the lower planes of double seismic zones caused by serpentine dehydration in subducting oceanic mantle?, *Geology*, *29*, 299–302.
- Peacock, S. M., and K. Wang (1999), Seismic consequences of warm versus cool subduction metamorphism: Examples from southwest and northeast Japan, *Science*, *186*, 937–939.
- Preston, L. A., K. C. Creager, R. S. Crosson, T. M. Brocher, and A. M. Trehu (2003), Intraslab earthquakes: Dehydration of the Cascadia slab, *Science*, *302*, 1197–1200.
- Ramachandran, K., R. D. Hyndman, and T. M. Brocher (2006), Regional *p* wave velocity structure of the Northern Cascadia Subduction Zone, *J. Geophys. Res.*, *111*, B12301, doi:10.1029/2005JB004108.
- Rogers, G., and H. Dragert (2003), Episodic tremor and slip on the Cascadia subduction zone: The chatter of silent slip, *Science*, *300*, 1942–1943.
- Rondenay, S., M. G. Bostock, and J. Shragge (2001), Multiparameter two-dimensional inversion of scattered teleseismic body waves: 3. Application to the Cascadia 1993 data set, *J. Geophys. Res.*, *106*, 30,795–30,807.
- Rondenay, S., G. A. Abers, and P. E. van Keken (2008), Seismic imaging of subduction zone metamorphism, *Geology*, *36*, 275–278, doi:10.1130/G24112A.1.
- Rossi, G., G. A. Abers, S. Rondenay, and D. H. Christensen (2006), Unusual mantle Poisson's ratio, subduction, and crustal structure in central Alaska, *J. Geophys. Res.*, *111*, B09311, doi:10.1029/2005JB003956.
- Rubinstein, J. L., M. La Rocca, J. E. Vidale, K. Creager, and A. G. Wech (2007a), Tidal modulation of nonvolcanic tremor, *Science*, *319*, 186–189.
- Rubinstein, J. L., J. E. Vidale, J. Gomberg, P. Bodin, K. C. Creager, and S. D. Malone (2007b), Non-volcanic tremor driven by large transient shear stresses, *Nature*, *448*, 579–582, doi:10.1038/nature06017.
- Schimmel, M., and H. Paulssen (1997), Noise reduction and detection of weak, coherent signals through phase-weighted stacks, *Geophys. J. Int.*, *130*, 497–505.
- Schwartz, S. Y., and J. M. Rokosky (2007), Slow slip events and seismic tremor at circum-Pacific subduction zones, *Rev. Geophys.*, *45*, RG3004, doi:10.1029/2006RG000208.
- Shelly, D. R., G. C. Beroza, and S. Ide (2006), Low-frequency earthquakes in Shikoku, Japan, and their relationship to episodic tremor and slip, *Nature*, *442*, 488–491.
- Shelly, D. R., G. C. Beroza, and S. Ide (2007a), Non-volcanic tremor and low-frequency earthquake swarms, *Nature*, *446*, 305–307.
- Shelly, D. R., G. C. Beroza, and S. Ide (2007b), Complex evolution of transient slip derived from precise tremor locations in western Shikoku, Japan, *Geochem. Geophys. Geosyst.*, *8*, Q10014, doi:10.1029/2007GC001640.
- Shiomi, K., H. Sato, K. Obara, and M. Ohtake (2004), Configuration of subducting Philippine Sea plate beneath southwest Japan revealed from receiver function analysis based on the multivariate autoregressive model, *J. Geophys. Res.*, *109*, B04308, doi:10.1029/2003JB002774.
- Szeliga, W., T. Melbourne, M. Santillan, and M. Miller (2008), GPS constraints on 34 slow slip events within the Cascadia subduction zone, 1997–2005, *J. Geophys. Res.*, *113*, B04404, doi:10.1029/2007JB004948.
- Tibi, R., D. A. Wiens, and X. Yuan (2008), Seismic evidence for widespread serpentinized forearc mantle along the Mariana convergence margin, *Geophys. Res. Lett.*, *35*, L13303, doi:10.1029/2008GL034163.
- Wang, K., and G. Rogers (1994), An explanation for the double seismic layers north of the Mendocino triple junction, *Geophys. Res. Lett.*, *21*, 121–124.
- Wang, K., J. F. Cassidy, I. Wada, and A. J. Smith (2004a), Effects of metamorphic crustal densification on earthquake size in warm slabs, *Geophys. Res. Lett.*, *31*, L01605, doi:10.1029/2003GL018644.
- Wang, K., I. Wada, and Y. Ishikawa (2004b), Stresses in the subducting slab beneath southwest Japan and relation with plate geometry, tectonic forces, slab dehydration, and damaging earthquakes, *J. Geophys. Res.*, *109*, B08304, doi:10.1029/2003JB002888.
- Wang, Z., D. Zhao, O. P. Mishra, and A. Yamada (2006), Structural heterogeneity and its implications for the low frequency tremors in southwest Japan, *Earth Planet. Sci. Lett.*, *251*, 66–78, doi:10.1016/j.epsl.2006.08.025.
- Wech, A. G., and K. C. Creager (2007), Cascadia tremor polarization evidence for plate interface slip, *Geophys. Res. Lett.*, *34*, L22306, doi:10.1029/2007GL031167.
- Wessel, P., and W. H. F. Smith (1991), Free software helps map and display data, *Eos Trans. AGU*, *72*, 441.
- Yamauchi, M., K. Hirahara, and T. Shibutani (2003), High resolution receiver function imaging of the seismic velocity discontinuities in the crust and the uppermost mantle beneath southwest Japan, *Earth Planets Space*, *55*, 59–64.
- Yuan, X., et al. (2000), Subduction and collision processes in the central Andes constrained by converted seismic phases, *Nature*, *408*, 958–961.
- Zandt, G., and C. J. Ammon (1995), Continental crust composition constrained by measurements of crustal Poisson's ratio, *Nature*, *374*, 152–154.
- Zhu, L., and H. Kanamori (2000), Moho depth variation in southern California from teleseismic receiver functions, *J. Geophys. Res.*, *105*, 2969–2980.

R. M. Allen and P. Audet, Seismological Laboratory, Department of Earth and Planetary Science, University of California, Berkeley, CA 94720, USA. (paudet@berkeley.edu)

M. G. Bostock, Department of Earth and Ocean Sciences, University of British Columbia, 6339 Stores Rd., Vancouver, BC V6T 1Z4, Canada.

D. C. Boyarko and M. R. Brudzinski, Department of Geology, Miami University, Oxford, OH 45056, USA.